Research Article

Composition optimization, high-temperature stability, and thermal cycling performance of Sc-doped Gd$_2$Zr$_2$O$_7$ thermal barrier coatings: Theoretical and experimental studies

Lei GUO[a,b,*], Bowen LI[a], Yuxian CHENG[c], Lu WANG[c]

[a]*School of Materials Science and Engineering, Tianjin University, Tianjin 300072, China*
[b]*Tianjin Key Laboratory of Advanced Joining Technology, Key Lab of Advanced Ceramics and Machining Technology of Ministry of Education, Tianjin 300072, China*
[c]*AECC Shenyang Liming Aero-Engine Co., Ltd., Shenyang 110043, China*

Abstract: Sc was doped into Gd$_2$Zr$_2$O$_7$ for expanding the potential for thermal barrier coating (TBC) applications. The solid solution mechanism of Sc in the Gd$_2$Zr$_2$O$_7$ lattice, and the mechanical and thermophysical properties of the doped Gd$_2$Zr$_2$O$_7$ were systematically studied by the first-principles method, based on which the Sc doping content was optimized. Additionally, Sc-doped Gd$_2$Zr$_2$O$_7$ TBCs with the optimized composition were prepared by air plasma spraying using YSZ as a bottom ceramic coating (Gd–Sc/YSZ TBCs), and their sintering behavior and thermal cycling performance were examined. Results revealed that at low Sc doping levels, Sc has a large tendency to occupy the lattice interstitial sites, and when the doping content is above 11.11 at%, Sc substituting for Gd in the lattice becomes dominant. Among the doped Gd$_2$Zr$_2$O$_7$, the composition with 16.67 at% Sc content has the lowest Pugh's indicator (G/B) and the highest Poisson ratio (σ) indicative of the highest toughness, and the decreasing trends of Debye temperature and thermal conductivity slow down at this composition. By considering the mechanical and thermophysical properties comprehensively, the Sc doping content was optimized to be 16.67 at%. The fabricated Gd–Sc coatings remain phase and structural stability after sintering at 1400 ℃ for 100 h. Gd–Sc/YSZ TBCs exhibit excellent thermal shock resistance, which is related to the good thermal match between Gd–Sc and YSZ coatings, and the buffering effect of the YSZ coating during thermal cycling. These results revealed that Sc-doped Gd$_2$Zr$_2$O$_7$ has a high potential for TBC applications, especially for the composition with 16.67 at% Sc content.

Keywords: thermal barrier coating (TBC); first-principles calculation; solid solution mechanism; high-temperature stability; thermal cycling

---

* Corresponding author.
E-mail: glei028@tju.edu.cn

1 Introduction

Thermal barrier coating (TBC) is a kind of high-temperature protective coating used for aero turbine engine blades, prolonging blade working lifetime and improving thrust to weight ratio and thermal efficiency [1–3]. TBCs are generally composed of a ceramic topcoat, thermally grown oxide (TGO), bond coat, and superalloy substrate. The ceramic topcoat generally has the properties of low thermal conductivity, high chemical stability and thermal expansion coefficient (TEC) to meet the requirements of reducing the surface temperature of the substrate and the thermal mismatch between the TBC and the substrate [4,5]. The traditional ceramic topcoat material is Y_2O_3 partially stabilized ZrO_2 (YSZ), which has good thermal and mechanical properties [6–8]. However, a transition from metastable tetragonal phase (t′) to monoclinic phase (m) occurs when YSZ is in long-term service above 1200 ℃, which is often accompanied by volume expansion, resulting in coating spallation. In addition, YSZ has sintering shrinkage and other problems during the long-term service, which greatly reduces the thermal insulation performance of the coating [4,9].

In recent years, rare earth zirconates ($RE_2Zr_2O_7$, RE = rare earth element) have been widely concerned by many scholars. Because of their low thermal conductivity, high TEC, and good phase stability, they are a series of good candidates for TBC applications. Among $RE_2Zr_2O_7$, $Gd_2Zr_2O_7$ has the lowest thermal conductivity (1.2 W/(m·K)) and the highest TEC (10.76×10^{-6} K^{-1}) [10–12]. Note that the thermal conductivity and TEC of YSZ are 2.03 W/(m·K) and 11.15×10^{-6} K^{-1}, respectively. Thus, $Gd_2Zr_2O_7$ has been regarded as one of the most promising TBC materials [13,14]. In addition, $Gd_2Zr_2O_7$ has low oxygen permeability and structural stability at high temperatures [15]. However, the mechanical properties of $Gd_2Zr_2O_7$ are poor, which limits its application.

$Gd_2Zr_2O_7$ has two crystal structures, namely pyrochlore structure and defect fluorite structure, both of which are face centered cubic space lattice [16,17]. Gd^{3+} and Zr^{4+} lattice sites can be replaced by other ions, and some small ions could also enter the interstitial sites. Due to the difference in size, mass, and force between doping atoms and Gd^{3+}, phonon scattering in the doped $Gd_2Zr_2O_7$ lattice could be enhanced. Therefore, the thermal conductivity of $Gd_2Zr_2O_7$ can be further reduced by selectively doping other ions in the $Gd_2Zr_2O_7$ lattice, and other thermophysical and mechanical properties can also be improved. It is reported that the TEC of $RE_2Zr_2O_7$ increases with the decrease of RE^{3+} (rare earth) size [18]. Zhang *et al.* [13] found that the fracture toughness of $Gd_2Zr_2O_7$ can be increased by doping Yb^{3+}. Lee *et al.* [19] found that the doping Y^{3+} can significantly improve hardness, elastic modulus, and insulation performance of $Gd_2Zr_2O_7$. These results show that doping small RE^{3+} in $Gd_2Zr_2O_7$ is beneficial to improve toughness, hardness, elastic modulus, and thermophysical properties. Among the RE^{3+}, Sc^{3+} has the smallest radius. Our previous research results showed that the addition of Sc^{3+} can increase the fracture toughness and TEC of $Gd_2Zr_2O_7$ [20–22]. However, in previous studies, the doping amount of Sc was not optimized, and the solid solution mechanism of Sc in $Gd_2Zr_2O_7$ lattice was not clarified theoretically.

Thermal shock resistance behavior, sintering resistance, and phase stability of TBCs at high temperature are of great theoretical significance for the optimization design of aeroengine. $RE_2Zr_2O_7$ coating is resistant to sintering at high temperatures, and is not easy to undergo phase transformation, but its fracture toughness and TEC are relatively low, which would lead to poor thermal shock lifetime. Karabaş [23] found that the thermal cycle life of $La_2Zr_2O_7$ can be improved by doping rare earth elements. Zhang *et al.* [24] studied the high-temperature stability and thermal shock resistance of $(Gd_{0.9}Yb_{0.1})_2Zr_2O_7$ TBCs, and found that they can still maintain good phase stability at 1600 ℃, and have excellent thermal cycle performance. Other studies have shown that the design of double-ceramic-layer (DCL) TBC structure can also improve the thermal shock lifetime, and YSZ coating can effectively alleviate the thermal stress at high temperature [25–27]. According to the above reports, $RE_2Zr_2O_7$ materials have good phase stability at high temperatures, and the thermal shock resistance can be improved by doping rare earth elements.

The first-principles calculation method based on density functional theory has developed into an important method to predict the properties of materials in recent years, and has been used by many scholars to study the effect of rare-earth doping on the properties of rare earth zirconate [11,12,28,29]. Li *et al.* [29] found by first-principles calculation that doping Sm^{3+} in $La_2Zr_2O_7$ could improve the mechanical and thermal properties, and $LaSmZr_2O_7$ has the optimal mechanical and thermal properties when the Sm content is 50 at%.

Zhao *et al.* [11] used density functional theory and found that the Young's modulus, Debye temperature, and thermal conductivity of $Gd_2Zr_2O_7$ decrease with the Th content. Zhao *et al.* [12] used first-principles calculation method, and found that the Young's modulus of $Gd_2Zr_2O_7$ decreases by 22.2–59.9 GPa with the Ce content, and the thermal conductivity decreases by 21% after completely replacing Ce at Zr site. However, the above doping models were established by replacing the RE-site or Zr-site in the pyrochlore lattice, and the interstitial model is not studied. Additionally, the solid solution mechanisms of doped atoms have not been analyzed completely.

Sc has been proved to be a very effective dopant, which can significantly improve the mechanical and thermal properties of $Gd_2Zr_2O_7$, but its solution mechanism and optimal doping amount are still unclear. For TBC's application, the thermal shock and sintering behavior need to be investigated. Therefore, this study intends to clarify the solution mechanism of Sc-doped $Gd_2Zr_2O_7$ by the first-principles method, optimize the Sc doping amount by considering the mechanical and thermophysical properties, and investigate the sintering and thermal shock behavior of Sc-doped $Gd_2Zr_2O_7$ TBCs.

2 Theoretical calculation methods and experimental procedure

2. 1 Theoretical calculation method

The theoretical calculations were carried out by the Vienna Ab initio Simulation Package (VASP) software based on density functional theory (DFT) [30]. The projector augmented wave (PAW) method was used to describe the interaction between electrons and ions, and the generalized gradient approximation (GGA) was used to describe the electron exchange correlation potential [31,32]. In all calculations, the plane wave cutoff energy was set to 500 eV and the k-point is $3 \times 3 \times 3$. The convergence criterion of structural optimization was that the stress of each atom was less than 0.01 eV/atom. In this work, $Gd_2Zr_2O_7$ pyrochlore structure was first established, and then several possible models of Sc-doped $Gd_2Zr_2O_7$ solid solution was examined. For the strong interactions caused by the 4f electrons of Gd, we did not adopt the Hubbard U correction method. The 4f electrons are regarded as core states,

because 4f electrons do not affect the calculated results of mechanical and thermodynamic properties [33,34].

In order to elucidate the solid solution mechanism of Sc atom in $Gd_2Zr_2O_7$ lattice, the defect formation energies of different doping models were calculated based on Eq. (1) [35]:

$$E_f = E_{tot}[\text{defect}] - E_{bulk}[\text{perfect}] - \sum_i n_i \mu_i \qquad (1)$$

where $E_{tot}[\text{defect}]$ is the energy of the crystal after doping, $E_{bulk}[\text{perfect}]$ is the energy of an undoped perfect crystal, n_i is the number of doping atom i (if this atom is added to the system, $n > 0$, and if this atom is removed from the system, $n < 0$), and μ is the chemical potential of the corresponding atom.

After calculating the mechanical property parameters, the thermophysical properties were obtained, including longitudinal sound velocity v_l, transverse sound velocity v_t, average sound velocity v_m, Debye temperature Θ, and minimum thermal conductivity k_{min}. The formulas used are as Eqs. (2)–(5) [11,12]:

$$v_l = \sqrt{\left(B + \frac{4}{3}G\right)/\rho} \qquad (2)$$

$$v_t = \sqrt{G/\rho} \qquad (3)$$

$$v_m = \left[\frac{1}{3}\left(\frac{2}{v_l^3} + \frac{1}{v_t^3}\right)\right]^{-\frac{1}{3}} \qquad (4)$$

$$\Theta = \frac{h}{k_B}\left[\frac{3n}{4\pi}\left(\frac{N_A\rho}{M}\right)\right]^{\frac{1}{3}} v_m \qquad (5)$$

The minimum thermal conductivity is calculated by Clarke's model and Cahill's model with Eqs. (6) and (7), respectively [11,12]:

$$k_{min}^{\text{Clarke}} = 0.87 k_B M_a^{-\frac{2}{3}} E^{\frac{1}{2}} \rho^{\frac{1}{6}} \qquad (6)$$

$$k_{min}^{\text{Cahill}} = \frac{k_B}{2.48}\left(\frac{n}{V}\right)^{\frac{2}{3}} (v_l + 2v_t) \qquad (7)$$

where B is the bulk modulus, G is the shear modulus, E is the Young's modulus, ρ is the density, n is the number of atoms in the crystal, V_m is the volume of unit cell, h is the Planck constant, N_A is the Avogadro constant, k_B is the Boltzmann constant, M is the molar mass, and M_a is the average mass per atom.

2. 2 Experimental procedure

Sc-doped $Gd_2Zr_2O_7$ (Gd–Sc) powders were prepared by

a chemical precipitation and calcination method [36,37]. Firstly, Gd_2O_3, Sc_2O_3, and $ZrOCl_2 \cdot 8H_2O$ (99.9%, 1–3 μm; Jiangtian Chemical Reagents Co., Ltd., Tianjin, China) were weighed according to the molar ratio of 5:1:12. Gd_2O_3 and Sc_2O_3 were dissolved into excessive concentrated nitric acid (65%; Jiangtian Chemical Reagents Co., Ltd., Tianjin, China) to obtain $Gd(NO_3)_3$ and $Sc(NO_3)_3$ respectively, and $ZrOCl_2 \cdot 8H_2O$ was dissolved in deionized water. Then the solutions were mixed evenly and slowly dripped into excessive ammonia water with mechanically stirring and ultrasonic oscillated to obtain white precipitation, which was filtered and washed several times with deionized water and anhydrous ethanol until pH = 7 was reached. The obtained powders were dried at 120 ℃ for 10 h and calcined at 900 ℃ for 5 h for crystallization. Gd–Sc and YSZ powders were agglomerated into microscopic particles (38–92 μm) by a spray drying method before spraying (LGZ-3, Wuxi Dongsheng Spray-granulating and Drying Equipment Plant, Wuxi, China). The parameters of spray drying were as follows: The inlet and outlet temperatures were 240 and 100 ℃, respectively, and the feed rate was 100 g/min.

Gd–Sc coating and Gd–Sc/YSZ double-ceramic-layer coating (DCL) TBCs were produced by air plasma spraying (APS; Metro 7 M). The spraying parameters are shown in Table 1. The bond coat and the substrate were NiCoCrAlY (53–91 μm; Shenyang Liming Aero Engine Group Corporation Ltd., Shenyang, China) and Ni-based superalloy (DZ125, Shenyang Liming Aero Engine Group Corporation Ltd., Shenyang, China), respectively. Their compositions are listed in Table 2. When preparing the double-ceramic-layer coating,

Table 1 Plasma spray parameters of Gd–Sc/YSZ coatings

Parameter	Gd–Sc	YSZ
Current (A)	750	800
Power (kW)	28	30
Plasma gas, Ar/H_2 (SCFH)	80/4	80/4
Carrier gas, Ar (SCFH)	8	8
Spray distance (mm)	100	100

Table 2 Composition of NiCoCrAlY and Ni-based superalloy (DZ125)   (Unit: wt%)

	Ni	Co	Cr	Al	Y	W	Others
NiCoCrAlY	42.5	22.6	23.4	10	1.5	—	—
DZ125	59.6	10.1	9.1	5.2	—	6.8	9.2

YSZ coating was first sprayed on the bond coat, followed by the Gd–Sc coating. The preparation process of Gd–Sc/YSZ coating for the heat treatment experiment was as follows: The coating was prepared on a graphite substrate, and then the substrate was removed by heating at 800 ℃.

Thermal shock tests were conducted by a water quenching method. When the temperature of the furnace (SX-G05165, Tianjin Zhonghuan Experimental Electric Furnace Co., Ltd., Tianjin, China) was reached 1050 ℃, Gd–Sc TBCs and Gd–Sc/YSZ DCL TBCs were put into the furnace and held for 10 min, followed by putting it into deionized water to room temperature. This process was defined as one thermal cycle, and the termination condition was that the spallation area of the coating surface exceeds 20%. The sintering behavior of Gd–Sc/YSZ coatings was investigated at 1400 ℃ in a furnace (SK-G08163, Tianjin Zhonghuan Experimental Electric Furnace Co., Ltd., China) for 20, 50, 100, and 200 h. The porosity of the heat-treated coating was obtained by the microstructure image processing (MIP) software.

Phase compositions of samples were determined by an X-ray diffractometer (Bruker D8 Advanced, Germany) using Cu Kα radiation. The parameters were as follows: The voltage and current was 40 kV and 40 mA respectively, and the scanning range of 2θ was 20°–80° with a rate of 6 (°)/min. The high-temperature stability of Gd–Sc powders was examined by STA449C thermal analyzer, with the parameters as follows: The heating rate was 10 K/min, and the temperature range was from room temperature to 1450 ℃. The surface morphologies, cross-sectional microstructures, and composition analysis were observed by scanning electron microscope (SEM; Nanosem 430, FEI, USA) equipped with energy dispersive spectroscopy (EDS; IE 350).

3　Results and discussion

3. 1　Solid solution mechanism of Sc in $Gd_2Zr_2O_7$ lattice

The optimized $Gd_2Zr_2O_7$ model is shown in Fig. 1. The structure exhibits a typical pyrochlore structure with 16 Gd, 16 Zr, and 56 O atoms. In the lattice, Gd occupies 16d (0.5, 0.5, 0.5), Zr occupies 16c (0, 0, 0), and the O has two types of sites, i.e., 48f (x, 0.125, 0.125) and 8b (0.375, 0.375, 0.375). In addition, there is an unoccupied oxygen vacancy of 8a (0.125, 0.125, 0.125) in $Gd_2Zr_2O_7$ lattice.
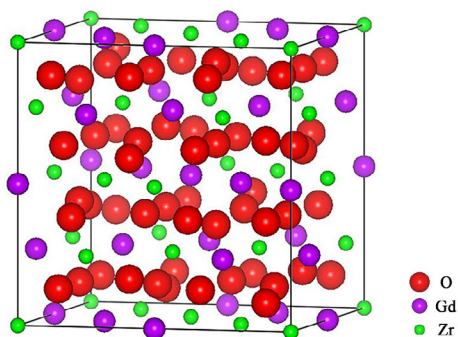
Fig. 1   Crystal structure of $Gd_2Zr_2O_7$.

The two most important parameters for describing the structure of pyrochlore are the lattice constant a_0 and the atomic coordinate parameter $x_{O\text{-}48f}$. The $x_{O\text{-}48f}$ is an important parameter for the degree of structural disorder, with a value between 0.3125 and 0.375 [38]. When $x_{O\text{-}48f} = 0.3125$, it is an ideal pyrochlore structure, while when $x_{O\text{-}48f} = 0.375$, the system exhibits a disordered fluorite structure, that is, a larger value of $x_{O\text{-}48f}$ means a more disordered lattice structure [39]. After completing structural relaxation, the results of a_0, $x_{O\text{-}48f}$, and density of the $Gd_2Zr_2O_7$ model are obtained as shown in Table 3, which are 10.600 Å, 0.3386, and 6.79 g/cm^3, respectively, showing agreement with the published values [40–43]. The above part demonstrates the reliability of our calculation results.

In $Gd_2Zr_2O_7$ lattice, the doped Sc has two possible sites, i.e., interstitial site and substitution for Gd. In order to determine the solid solution mechanism of Sc in the lattice, we established models with one Sc atom, two Sc atoms, three Sc atoms, and four Sc atoms, which were named $Gd_{Sc\text{-}1\text{-}inter}$ and $Gd_{Sc\text{-}1\text{-}sub}$, $Gd_{Sc\text{-}2\text{-}inter}$ and $Gd_{Sc\text{-}2\text{-}1\text{-}inter+1\text{-}sub}$, $Gd_{Sc\text{-}3\text{-}inter}$ and $Gd_{Sc\text{-}3\text{-}2\text{-}inter+1\text{-}sub}$, and $Gd_{Sc\text{-}4\text{-}2\text{-}inter+2\text{-}sub}$, respectively, as listed in Table 4 and shown in Fig. 2. The subscripts of "inter" and "sub" stand for a Sc atom occupying an interstitial site and substituting for Gd, respectively. The interstitial sites are 32e (0.25, 0.25, 0.25), which is the most stable interstitial site in pyrochlore structure [35]. The Gd site farthest from the 32e is selected as the substitution site.

Table 3   Structural parameters of $Gd_2Zr_2O_7$

	a_0 (Å)	$x_{O\text{-}48f}$	ρ (g/cm^3)
$Gd_2Zr_2O_7$	10.600	0.3386	6.79
Cal. [40]	10.682	0.338	6.629
Cal. [11]	10.452	0.342	—
Cal. [41]	10.66	0.339	—
Exp. [42]	10.54	0.344	6.8 [43]

Table 4   Lattice constants and formation energy calculations of Sc-doped $Gd_2Zr_2O_7$

	Sc content (at%)	a_0 (Å)	E_f (eV)
$Gd_{Sc\text{-}1\text{-}sub}$	6.25	10.581	1.269
$Gd_{Sc\text{-}1\text{-}inter}$	5.88	10.646	0.141
$Gd_{Sc\text{-}2\text{-}inter}$	11.11	10.663	0.659
$Gd_{Sc\text{-}2\text{-}1\text{-}inter+1\text{-}sub}$	11.76	10.632	0.745
$Gd_{Sc\text{-}3\text{-}inter}$	15.79	10.758	3.347
$Gd_{Sc\text{-}3\text{-}2\text{-}inter+1\text{-}sub}$	16.67	10.647	0.953
$Gd_{Sc\text{-}4\text{-}2\text{-}inter+2\text{-}sub}$	22.22	10.623	1.621

(a) $Gd_{Sc\text{-}1\text{-}inter}$ (b) $Gd_{Sc\text{-}1\text{-}sub}$

(c) $Gd_{Sc\text{-}2\text{-}1\text{-}inter+1\text{-}sub}$ (d) $Gd_{Sc\text{-}2\text{-}inter}$

(e) $Gd_{Sc\text{-}3\text{-}inter}$ (f) $Gd_{Sc\text{-}3\text{-}2\text{-}inter+1\text{-}sub}$

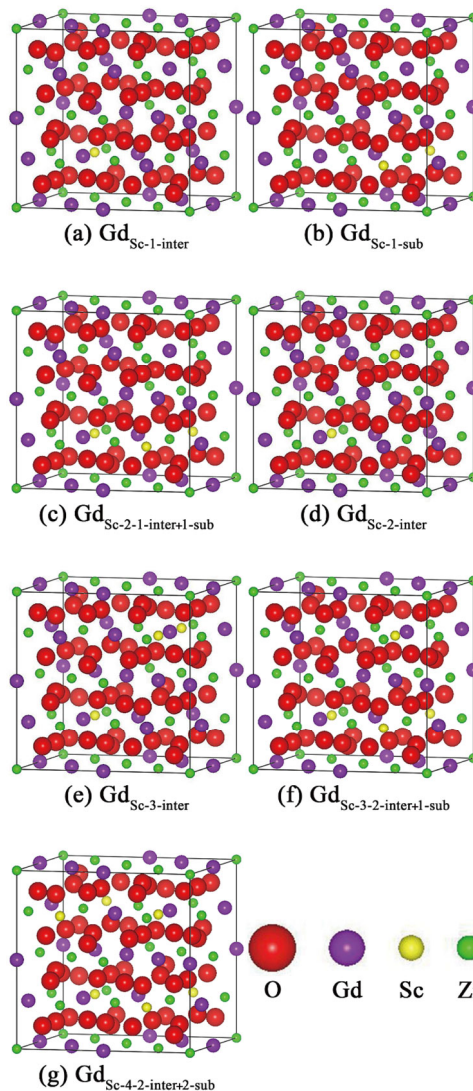(g) $Gd_{Sc\text{-}4\text{-}2\text{-}inter+2\text{-}sub}$

Fig. 2   Solid solution mode of Sc in $Gd_2Zr_2O_7$ lattice with different doping contents.

Defect formation energy is an important parameter to determine the mechanism of point defect formation, which has been widely used by many scholars to clarify the solid solution mechanism [35,44–46]. The smaller the value, the easier the doped atom can enter the lattice

[35,44–46]. The calculated formation energy values of above models are shown in Table 4. According to the calculation results, the solution mechanisms of Sc atoms in the $Gd_2Zr_2O_7$ lattice are analyzed as follows.

When the Sc content is low, Sc atoms mainly enter the interstitial sites of the lattice, because the formation energy of $Gd_{Sc-1-inter}$ (0.141) is obviously smaller than that of $Gd_{Sc-1-sub}$ (1.269), which is also consistent with our previous experimental results [20]. It is found that the formation energy of $Gd_{Sc-2-inter}$ is slightly lower than that of $Gd_{Sc-2-1-inter+1-sub}$, which indicates that there may be a tendency to substitute the Gd-site atoms at this Sc content. With the increase of Sc content, we found that the formation of $Gd_{Sc-3-inter}$ significantly increased, which means that the $Gd_2Zr_2O_7$ lattice has no ability to accommodate more interstitial Sc atoms; in the case of $Gd_{Sc-3-2-inter+1-sub}$ model, the formation energy decreases significantly, suggesting that substitution doping is dominant at this composition.

The calculated lattice constant values are also listed in Table 4, and shown in Fig. 3 with variation of the Sc contents. The lattice constant increases to 10.646 Å when the Sc content is below 11.11 at%, followed by a decrease. The increase is due to the dominant of interstitial Sc atoms causing lattice expansion, and the decrease could be attributed to the smaller Sc substitution for Gd. Note that when the Sc content is above 5.88 at%, the increase rate of lattice constant is reduced. This indicates that some Sc atoms have some possibility to substitute for Gd, offsetting the lattice expansion, which agrees with the formation energy calculation results. As a result, one could conclude that the interstitial Sc concentration in $Gd_2Zr_2O_7$ lattice might be less than 11.11 at%, which is consistent with our previous experimental results [18].

According to the change trend of the defect formation energy and lattice constant, the solid solution mechanism
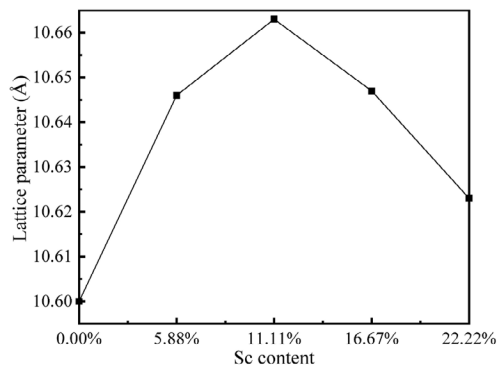

Fig. 3 Variations of lattice constant with the Sc content.

of Sc in $Gd_2Zr_2O_7$ lattice might be clear: When the Sc content is 5.88 at%, interstitial doping is dominant; when the Sc content is 5.88–11.11 at%, the interstitial Sc atoms reach saturation and there is a tendency to replace Gd atoms, after which the substitution doping begins to dominate gradually.

3. 2 Mechanical and thermophysical properties of Sc-doped $Gd_2Zr_2O_7$

Based on the fully optimized model, we calculated the mechanical properties of Sc-doped $Gd_2Zr_2O_7$ with $Gd_{Sc-1-inter}$, $Gd_{Sc-2-inter}$, $Gd_{Sc-3-2-inter+1-sub}$, and $Gd_{Sc-4-2-inter+2-sub}$, including elastic constants, bulk modulus B, shear modulus G, and Young's modulus E. For cubic system, there are three independent elastic constants C_{11}, C_{12}, and C_{44}. The calculated results are shown in Table 5. For $Gd_2Zr_2O_7$, there are some differences between our calculated results and values in the literature [12,34]. The reason may be that the pseudopotential we used is different from that in the literature. For the ceramic system, we did not consider the spin polarization in the calculation process, while the results in the literature considered it [12,34]. However, for the bulk elastic modulus B, shear elastic modulus G, and Young's elastic modulus E, our calculated results are in good agreement with the experimental values, which reveals the reliability of our calculated results.

The variation trends of elastic constant and elastic modulus with the Sc content are shown in Fig. 4, and the calculation results are listed in Table 5. It can be seen from Fig. 4(a) that C_{11}, C_{12}, and C_{44} all decrease in different degrees after doping Sc atoms. This phenomenon suggests that the addition of Sc is beneficial to improve the mechanical properties of $Gd_2Zr_2O_7$. For the cubic system, the elastic constants C_{11}, C_{12}, and C_{44} must meet the following three criteria to be mechanically stable: $C_{11} + 2C_{12} > 0$; $C_{44} > 0$; $C_{11} - C_{12} > 0$ [47]. According to the calculation results in Table 5, all models are satisfied, which indicates that the Sc-doped $Gd_2Zr_2O_7$ systems are all mechanically stable. In order to optimize the amount of Sc doping, we calculated the elastic modulus based on the result of the elastic constant, and the formula is as follows: $B = (C_{11} + 2C_{12})/3$, $G = \{(C_{11} - C_{12} + 3C_{44})/5 + 5(C_{11} - C_{12})C_{44}/[4C_{44} + 3(C_{11} - C_{12})]\}/2$, $E = 9BG/(3B + G)$ [11,12].

Figure 4(b) shows the bulk modulus B, shear modulus G, and Young's modulus E. With the increase of the content, bulk modulus B first decreases and then increases slowly. The shear modulus G decreases gently

Table 5   Elastic constant and elastic modulus of Sc-doped Gd$_2$Zr$_2$O$_7$

	C_{11} (GPa)	C_{12} (GPa)	C_{44} (GPa)	B (GPa)	G (GPa)	E (GPa)
Gd$_2$Zr$_2$O$_7$	296.521	101.943	86.824	166.803	90.869	230.712
Cal. [11]	324.7	125.3	94	191.8	96.2	247.3
Cal. [34]	277	110	52	165	63	214
Exp. [52]	—	—	—	174	93	236
Exp. [12]	—	—	—	153	80	205
Gd$_{Sc-1-inter}$	263.328	69.894	48.769	123.007	66.713	169.497
Gd$_{Sc-2-inter}$	285.407	81.656	55.201	147.880	69.716	180.745
Gd$_{Sc-3-2-inter+1-sub}$	281.431	99.205	58.998	154.205	62.964	166.263
Gd$_{Sc-4-2-inter+2-sub}$	273.801	86.689	53.527	140.88	60.089	157.827
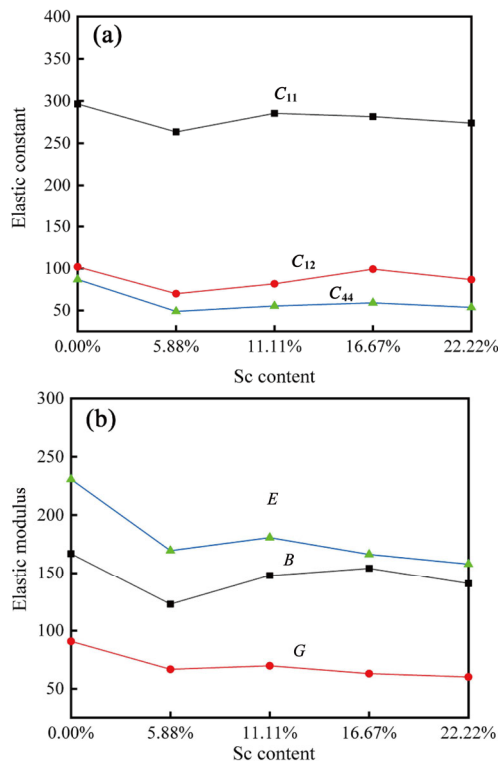
Fig. 4   Variations of (a) elastic constants C_{11}, C_{12}, C_{44}, and (b) bulk modulus B, shear modulus G, and Young's modulus E with the Sc content.

with the increase of Sc content, which is consistent with the research results of Th-doped Gd$_2$Zr$_2$O$_7$, Ti-doped Gd$_2$Zr$_2$O$_7$, and La-doped Gd$_2$Zr$_2$O$_7$ [11,12]. Note that doping Sc atom could reduce Young's modulus E by 50–73 GPa. This is because doping smaller Sc atom into Gd$_2$Zr$_2$O$_7$ lattice introduces size and coupling force mismatch, which causes fluctuation of strain field and lattice softening, resulting in a significant decrease of Young's modulus [48]. For TBC applications, a low Young's modulus is desirable, which means large strain tolerance of coatings beneficial for thermal shock

resistance of TBCs [49]. According to the results of elastic modulus, one could be found that the decreasing trends of Young's modulus E and shear modulus G slow down after 16.67 at% Sc content. Therefore, based on the calculation results of elastic modulus, the Sc content of 16.67 at% is the best.

The calculated results of Pugh's indicator (G/B) and Poisson ratios (σ) of Sc-doped Gd$_2$Zr$_2$O$_7$ with Gd$_{Sc-1-inter}$, Gd$_{Sc-2-inter}$, Gd$_{Sc-3-2-inter+1-sub}$, and Gd$_{Sc-4-2-inter+2-sub}$ are listed in Table 6. G/B is an important index to describe brittle toughness of materials, with a critical value of 0.5, above which the material exhibits brittleness [50]. In other words, the lower the G/B is, the better toughness the material has. Poisson's ratio σ is also an important parameter to describe the toughness of materials. For ductile materials, the Poisson's ratio is 0.33, while for strong covalent crystals, the Poisson's ratio is 0.1 [51]. In other words, a higher Poisson's ratio means better toughness of materials. The calculated G/B and Poisson's ratio of Gd$_2$Zr$_2$O$_7$ are 0.545 and 0.269 respectively, which are in good agreement with the literature values [11,52]. Figure 5 shows the variation of Pugh's indicator (G/B) and Poisson's ratio (σ) with the Sc content. With the increase of the Sc content, G/B decreases first followed by an increase when the

Table 6   Pugh's indicator (G/B) and Poisson's ratio (σ) of Sc-doped Gd$_2$Zr$_2$O$_7$

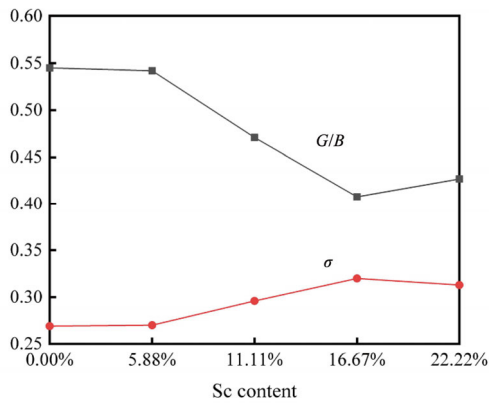|	G/B	σ
Gd$_2$Zr$_2$O$_7$	0.545	0.269
Cal. [11]	0.500	0.285
Exp. [52]	0.530	0.273
Gd$_{Sc-1-inter}$	0.542	0.270
Gd$_{Sc-2-inter}$	0.471	0.296
Gd$_{Sc-3-2-inter+1-sub}$	0.408	0.320
Gd$_{Sc-4-2-inter+2-sub}$	0.427	0.313

Fig. 5 Variations of Pugh's indicator (*G*/*B*) and Poisson's ratio (*σ*) with the Sc content.

doping content reaches 16.67 at%, while *σ* increases first and then shows a decrease. At a Sc doping level of 16.67 at%, *G*/*B* has the lowest value of 0.408, and *σ* has the highest value of 0.32, suggesting that the material with this composition has the highest toughness.

The thermophysical properties of different Sc-doped $Gd_2Zr_2O_7$ models are listed in Table 7. The calculated Debye temperature of $Gd_2Zr_2O_7$ is 508.506 K, which is close to the calculated value of 520.7 K by Zhao *et al.* [11] and the experimental 513.4 K by Shimamura *et al.* [52]. After doping Sc atoms into $Gd_2Zr_2O_7$, longitudinal sound velocity v_l, transverse sound velocity v_t, and average sound velocity v_m all decrease, which leads to the decrease of Debye temperature. The variation of Debye temperature *Θ* and thermal conductivity with the Sc content is shown in Fig. 6. 5.88 at% Sc doping into $Gd_2Zr_2O_7$ lattice reduces the Debye temperature by 72 K, while there is a slight increase in the Debye temperature when the doping content reaches 11.11 at%, and then it decreases again. Note that when Sc content exceeds 16.67 at%, the decreasing trend of Debye temperature slows down. Debye temperature of a material can reflect its TEC [53]. A low Debye temperature suggests weak interaction between atoms in the lattice, which indicates a high coefficient of thermal expansion
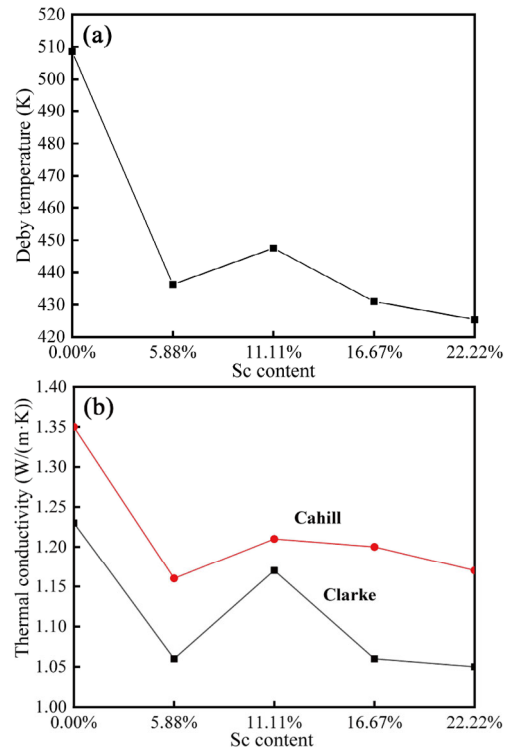
Fig. 6 Variation of (a) Debye temperature *Θ* and (b) thermal conductivity with the Sc content.

[12]. For TBC materials, a high coefficient of thermal expansion benefits to reduce the thermal mismatch between the coating and substrate.

The minimum thermal conductivities were calculated based on Cahill's model and Clarke's model as listed in Table 7, which are present in Fig. 6(b) as the function of the Sc content. The calculated thermal conductivities of $Gd_2Zr_2O_7$ are 1.23 W/(m·K) by Clarke's model and 1.35 W/(m·K) by Cahill's model, which are in agreement with the calculated value of 1.29 and 1.35 W/(m·K) by Zhao *et al.* [11,12]. Our calculated results are also within the experimental results range of 1.0–1.6 W/(m·K) [54–56]. It can be seen from Fig. 6(b) that the minimum thermal conductivity calculated by Cahill's model is slightly higher than that obtained

Table 7 Thermophysical properties of Sc-doped $Gd_2Zr_2O_7$

	v_l (m/s)	v_t (m/s)	v_m (m/s)	*Θ* (K)	k_{Clarke} (W/(m·K))	k_{Cahill} (W/(m·K))
$Gd_2Zr_2O_7$	6512.44	3658.179	4070.692	508.506	1.23	1.35
Cal. [11]	—	—	4108.0	520.7	1.29	1.42
Exp.	—	—	—	513.4 [52]	1.0–1.6 [54–56]	
$Gd_{Sc-1-inter}$	5595.406	3139.157	3493.509	436.277	1.06	1.16
$Gd_{Sc-2-inter}$	5955.415	3204.201	3577.345	447.505	1.17	1.21
$Gd_{Sc-3-2-inter+1-sub}$	5968.192	3068.724	3436.649	430.97	1.06	1.20
$Gd_{Sc-4-2-inter+2-sub}$	5809.301	3029.188	3389.289	425.403	1.05	1.17

Clarke's model, which is also in line with the calculation trend of other scholars [11,12]. The reason can be attributed to the consideration of phonon spectrum in Cahill's model while the lacking contribution of optical phonon in Clarke's model [57]. Comparing curves in Figs. 6(a) and 6(b), it could be found that the variation trend of thermal conductivity is similar with that of Debye temperature with the increase of Sc content. Based on Clarke's model, which is more suitable for insulators [58,59], one could be found that the decreasing trend slows down when the Sc content exceed 16.67 at%. It can be seen from the variation of Debye temperature and thermal conductivity that too much Sc doping (> 16.67 at%) has no obvious effect on increasing TEC and decreasing thermal conductivity.

The minimum thermal conductivity could be used as an approximation of the real thermal conductivity, which is related to the phonon scattering [24,60,61]. When the Sc content is 5.88 at%, Sc atoms mainly enter the interstitial sites of $Gd_2Zr_2O_7$, which enhances phonon scattering. However, in order to balance the charge, oxygen vacancies are consumed, which would reduce the phonon scattering. Note that the thermal conductivity is still greatly reduced, which indicates that interstitial doping atoms play a significant role in enhancing phonon scattering. With the increase of Sc content, Gd^{3+} is gradually replaced by Sc^{3+}. Due to that the smaller Sc^{3+} replaces Gd^{3+}, Sc^{3+} is loosely bound in an oversized atomic cage and does not easily vibrate with other phonons, acting like a local "rattler", which enhances the scattering of phonons and leads to a decrease in the thermal conductivity. However, its enhancement effect is not as significant as that brought by interstitial atoms, which leads to a slow decline in thermal conductivity [62].

According to the theoretical calculation, the mechanical and thermophysical properties of $Gd_2Zr_2O_7$ can be designed by Sc doping. When the Sc content is less than 11.11 at%, the interstitial doping of Sc atoms is dominant. Then, the Gd^{3+} sites would be gradually replaced by Sc^{3+} with the increase of Sc content. Young's modulus decreases by 50–64 GPa after doping Sc atom, which benefits the thermal shock resistance and high-temperature stability of the coating. When the content of Sc exceeds 16.67 at%, the decreasing trends of Young's modulus and shear modulus slow down. The toughness of the material can be improved obviously by doping Sc atoms, and when Sc content is 16.67 at%, the toughness reaches the optimum. Similarly, the downward trends of Debye temperature and thermal conductivity begin to slow down after Sc content exceeds 16.67 at%. Therefore, when the content of Sc is about 16.67 at%, all aspects of the performance are the most suitable.

3.3 Preparation of Gd–Sc TBCs and their sintering behavior

The XRD patterns of the prepared Gd–Sc powders, Gd–Sc TBCs, and Gd–Sc/YSZ DCL TBCs (Sc content is 16.67 at%) are shown in Fig. 7(a). All the patterns exhibit similar appearance, which have diffraction peaks ascribed to disordered defect fluorite. This indicates that during plasma spraying processes, Gd–Sc powders keep phase stability, and our spraying parameters are suitable. Figure 7(b) shows the DSC curve of Gd–Sc powders at a temperature range of 25–1450 ℃. There is an endothermic peak at 388 ℃, which may be caused by evaporative heat absorption of crystalline water. No other heat absorption or exothermic peaks can be observed during the whole heating process, which indicates that Gd–Sc can maintain good high-temperature stability up to 1450 ℃. This is beneficial for Gd–Sc coatings used at elevated temperatures.
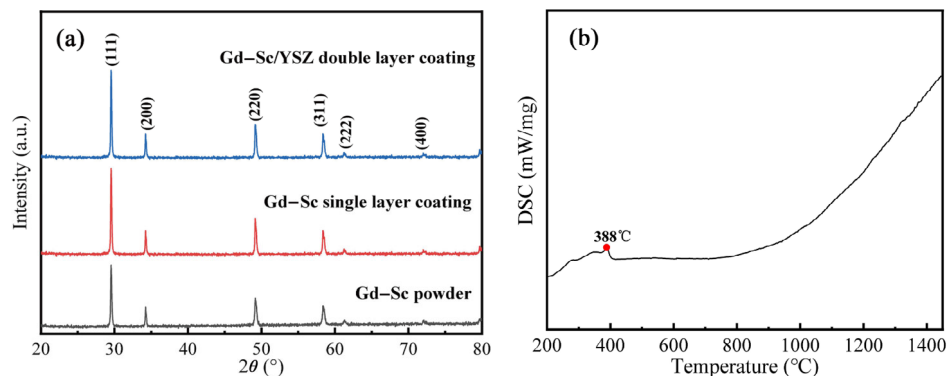
Figure 8(a) shows the surface morphology of Gd–Sc

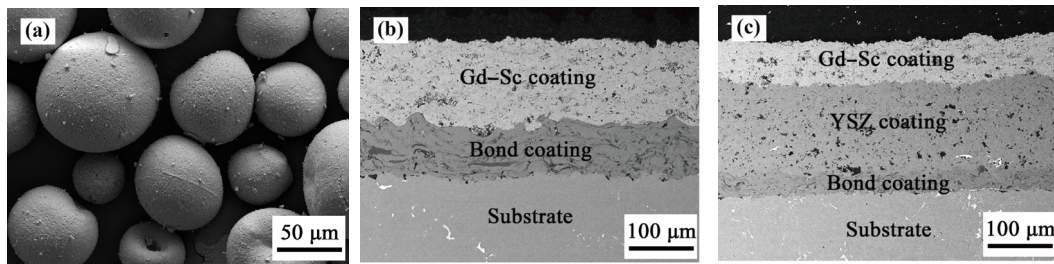**Fig. 7** (a) XRD patterns of Gd–Sc powders and coatings, and (b) DSC curve of Gd–Sc powders.

Fig. 8 (a) Surface morphology of Gd–Sc spraying powders, and cross-sectional microstructures of (b) Gd–Sc TBC and (c) Gd–Sc/YSZ DCL TBC.
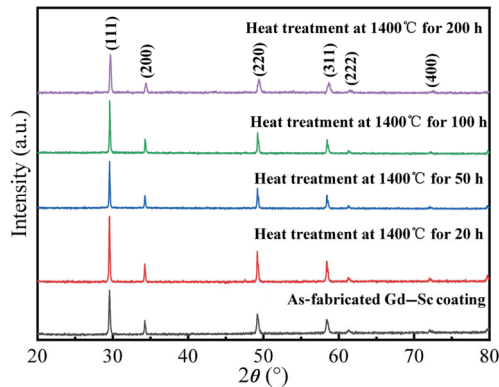

Fig. 9 XRD patterns of Gd–Sc coatings after different heat treatment time.

spraying powders. The powders exhibit a spherical appearance, and the size is 38–76 μm. Cross-sectional microstructures of Gd–Sc TBCs and Gd–Sc/YSZ DCL TBCs are shown in Figs. 8(b) and 8(c), respectively. The Gd–Sc coating and YSZ coating show a typical layered structure, and both types of TBCs have integral interface, where there are no obvious defects such as gaps and cracks. In Gd–Sc TBCs, the thickness of the Gd–Sc coating is ~120 μm. In Gd–Sc/YSZ DCL TBCs, the thickness of Gd–Sc coating is ~80 μm and that of YSZ coating is ~150 μm.

The XRD patterns of Gd–Sc/YSZ coatings after heat treatment tests at 1400 ℃ are shown in Fig. 9. It can be seen that the patterns of the heat-treated coatings are similar to that of the as-fabricated coating except that the peaks become sharp, which indicates the crystallization degree of the coatings increases after heat treatments. No new phases are formed in the coatings during sintering, indicating that Gd–Sc coating has excellent phase stability at 1400 ℃.

The surface morphologies of Gd–Sc coatings after heat treatments at 1400 ℃ are shown in Fig. 10. During the first 100 h heat treatment, the coating surface morphologies have little change indicative of excellent sintering resistance. Prolonging the heat treatment to 200 h, many micro-cracks disappear and

some large cracks appear, and in the enlarged image (Fig. 10(d)), one can found that the grains have some growth. This indicates that the coating experiences some sintering during long-term heat treatment at 1400 ℃, but the sintering degree is not severe, and the coating almost keeps its original morphology. Additionally, the porosity values of heat-treated coatings (20, 50, 100, and 200 h) are 10.7%, 10.19%, 9.25%, and 8.19%, respectively. This suggests that the porosity of the coating decreases gradually with the extension of heat treatment time.

The fracture surface morphology of Gd–Sc coatings after heat treatments at 1400 ℃ are shown in Fig. 11. It can be seen that the layered structure can be clearly observed in the coatings after 20 h, 50 h, and 100 h heat treatments. When the heat treatment time is extended to 200 h, the lamellar structure is not obvious, microcracks and pores are closed, and some vertical cracks begin to appear, which indicates that the coating turns to sintering. The reason for the vertical cracks may be that sufficient temperature and time provide driving force for the growth of grains during heat treatment. At the beginning of sintering, grains contact with each other, resulting in sintering neck, and microcracks and voids gradually heal; with the extension of time to the later stage of sintering, the micro-cracks and voids disappear, which reduces the strain tolerance and thermal insulation of the coating. The thermal stress accumulated during long-term heat treatment could not be released through micro-cracks and voids, resulting in stress concentration, which results in cracks during the cooling phase. This would not benefit the thermal shock resistance, corrosion resistance, or other properties of the coating, and greatly reduces the service life of the coating.

3. 4   Thermal cycling behavior of Gd–Sc TBCs and Gd–Sc/YSZ DCL TBCs

The macroscopic morphology evolution of Gd–Sc TBCs and Gd–Sc/YSZ DCL TBCs during thermal cycling
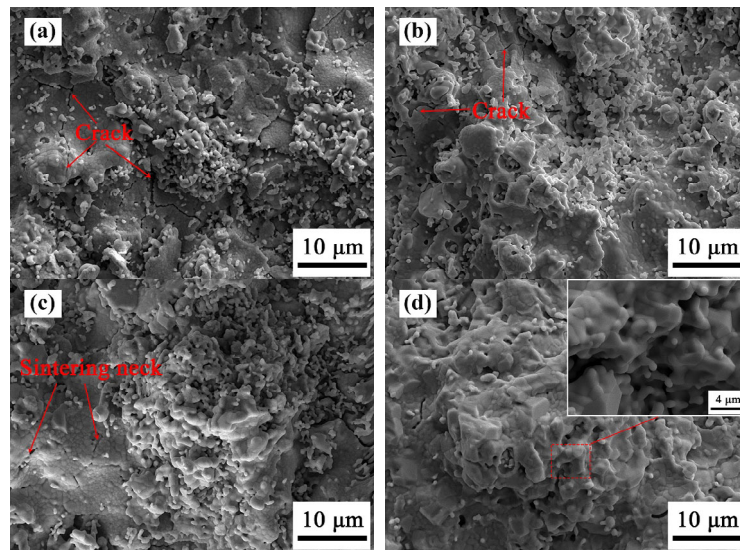
Fig. 10 Surface morphologies of Gd–Sc coatings after heat treatment at 1400 ℃ for (a) 20 h, (b) 50 h, (c) 100 h, and (d) 200 h.
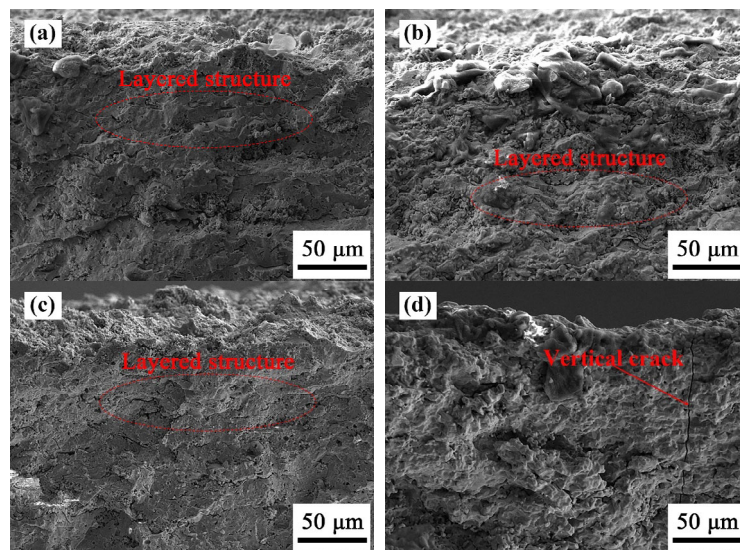

Fig. 11 Fracture surface morphologies of Gd–Sc coatings after heat treatment at 1400 ℃ for (a) 20 h, (b) 50 h, (c) 100 h, and (d) 200 h.

tests is shown in Fig. 12. Both types of TBCs spalled from the edge. After 75 and 215 thermal cycles, the spallation area of Gd–Sc TBCs and Gd–Sc/YSZ DCL TBCs reaches 20% of the total area, respectively. The superalloy substrates become black, which indicates that substrate oxidation takes place during the thermal cycling test. By comparison, Gd–Sc/YSZ DCL TBCs exhibit much longer lifetime than that of Gd–Sc TBCs, revealing that double-layer design could significantly improve the thermal shock resistance of TBCs.

The XRD patterns of the Gd–Sc TBCs and Gd–Sc/YSZ DCL TBCs after thermal cycling tests are shown in Fig. 13. During the tests, Gd–Sc coatings have no phase decomposition, indicating that the coatings have excellent phase stability. $AlNi_3$ is detected in the Gd–Sc
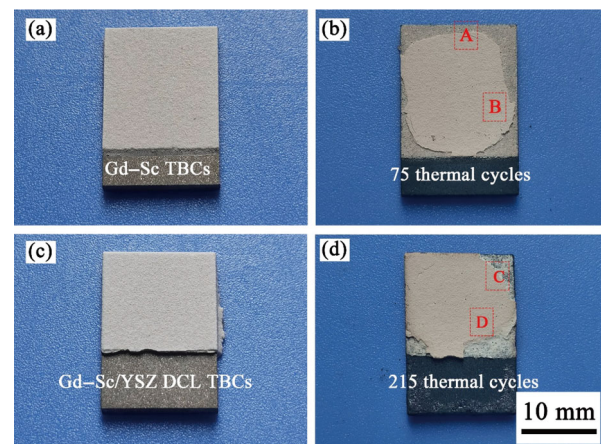
Fig. 12 Macroscopic morphology evolution of (a, b) Gd–Sc TBCs and (c, d) Gd–Sc/YSZ DCL TBCs during thermal cycling tests.
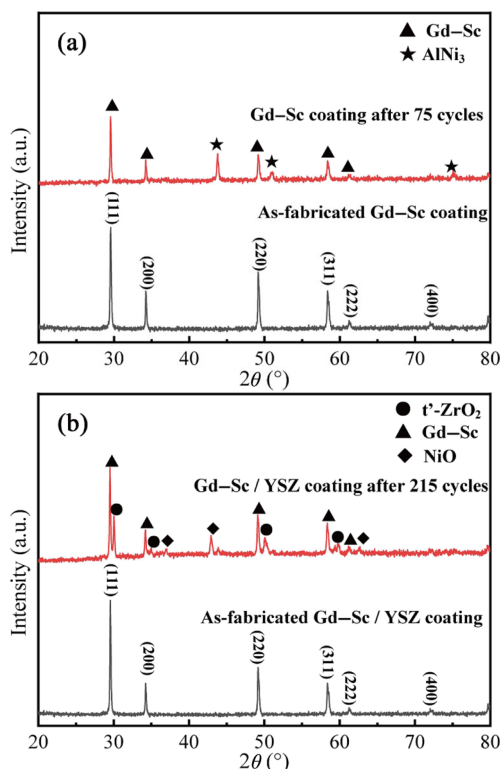
Fig. 13 XRD patterns of (a) Gd–Sc TBCs and (b) Gd–Sc/YSZ DCL TBCs after thermal cycling tests.

TBCs after 75 thermal cycles, which is the component of the bonding coating [63,64]. It could be presumed that some regions of Gd–Sc coating have spalled off, leaving the bond coat outside. After 215 thermal cycles, t'-ZrO$_2$ and NiO are detected in the Gd–Sc/YSZ DCL TBCs. This indicates that the spallation may occur near the bond coat, causing the TGO being detected.

The spalling edge region and adjacent region of Gd–Sc TBCs and Gd–Sc/YSZ DCL TBCs are marked as A, B, C, and D, respectively, as shown in Figs. 12(b) and 12(d). Figure 14(a) shows the cross-sectional morphology of region A. After 75 thermal cycles, the Gd–Sc coating has spalled, and there is a large delamination crack in the coating. The cross-sectional morphology of region B is shown in Fig. 14(b). It can be seen that the coating delamination starts from the region near the bond coat, and the thickness of TGO is ~5 μm. It has been reported that Gd$_2$Zr$_2$O$_7$ can react with TGO during heat treatment, which causes stress growth and crack formation at the interface between Gd$_2$Zr$_2$O$_7$ coating and the bond coat [25,65]. For Gd–Sc coating, it also has large possibility to react with TGO, resulting in delamination crack in the coating region near the bond coat. However, it is difficult to observe the reaction products, which may be due to the small amount. Additionally, although Gd–Sc has improved toughness compared with Gd$_2$Zr$_2$O$_7$, its toughness is still not high enough to resist the thermal stress generated in the thermal cycle process, which inevitably leads to the formation of cracks in the Gd–Sc coating.

Figure 15(a) shows the cross-sectional microstructure of region C. After 215 thermal cycles, the interface between Gd–Sc and YSZ coatings is well bonded, without any defect, and both coating maintains good structural integrity. However, a larger delamination crack forms in the YSZ coating, above which the coatings are spalled. The cross-sectional morphology of region D is shown in Fig. 15(b). Although the coatings here are not spalled, some delamination cracks can be found in the YSZ coating, which could cause coating spallation like Fig. 15(a) by further thermal shock. The EDS line scanning of the interface between Gd–Sc and YSZ coatings is shown in Fig. 15(c). It could be found that Gd and Sc elements do not diffuse into YSZ coating. This indicates that the Gd–Sc coating maintains good phase stability during thermal cycling test, which is also consistent with the results of the DSC. At the interface between the YSZ coating and the bond coat, some dark contrast products are observed, which are denoted as E. EDS analysis results show that the product is mainly composed of Ni, Al, O, and a small amount
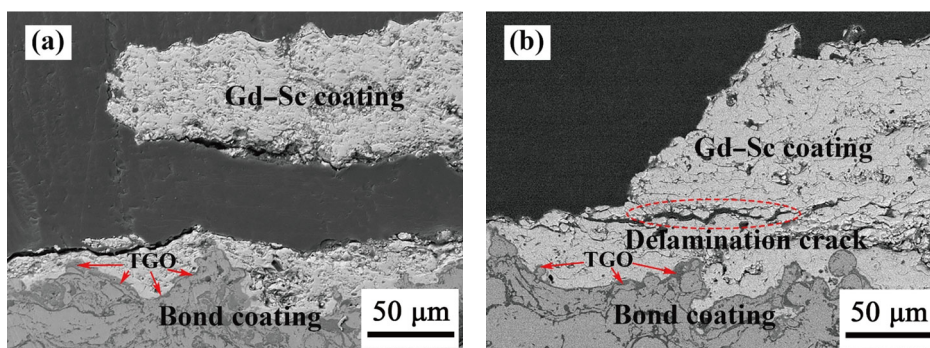

Fig. 14 Cross-sectional microstructures of regions (a) A and (b) B of Gd–Sc TBCs after 75 thermal cycles.
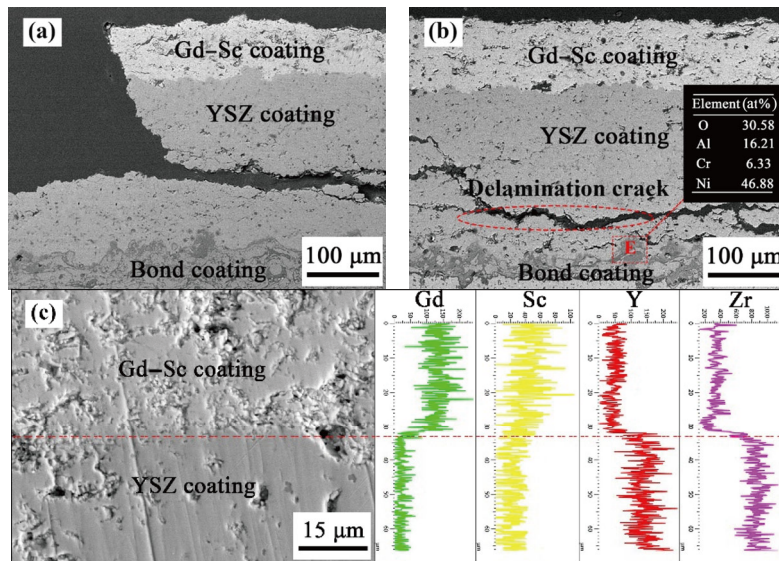
Fig. 15 Cross-sectional microstructures of regions (a) C and (b) D of Gd–Sc/YSZ DCL TBCs after 215 thermal cycles. (c) EDS line scanning of the interface between Gd–Sc and YSZ coating.

of Cr. Combined with the XRD results, we can determine that the products in this region are mainly NiO, as well as some Cr and Al oxides, which is the component of TGO.

Based on the results of SEM and EDS, the failure mechanisms of Gd–Sc/YSZ DCL TBCs could be analyzed as follows. Since the bottom and side of substrate are not covered with the coating, and the thickness of the bond coat is thin, which results in serious oxidation of the alloy substrates and bond coat during thermal cycling. The thickness of the TGO has increased to ~15 μm with a larger volume expansion, thereby producing a large stress concentration near the oxidation product, resulting in the initiation and propagation of cracks, which lead to the YSZ coating cracking. Note that Gd–Sc coating still maintains good structural integrity and the interface with YSZ coating is intact. This is because the doping of Sc improves the toughness and TEC, and reduces the Young's modulus, which ensures the tolerance in the process of thermal cycle, and has a good thermal match with YSZ. YSZ coating plays a good buffer role during thermal cycling, and prevents the reaction of Gd–Sc with the bond coat to form $GdAlO_3$ phase.

Additionally, Gd–Sc/YSZ DCL TBCs have a thicker ceramic layer and a thinner bond coat than Gd–Sc TBCs. It has been reported that the thermal shock resistance of TBCs decreases with the increase of ceramic coat thickness [66]. A thin bond coat can lead to premature oxidation during the thermal cycle, resulting in the premature failure of the coating [67]. Generally

speaking, Gd–Sc/YSZ DCL TBCs should have a lower thermal cycling life in theory due to a thicker ceramic layer and a thinner bond coat. However, the thermal cycling life of Gd–Sc/YSZ DCL TBCs is still three times that of Gd–Sc TBCs, which indicates that Gd–Sc/YSZ DCL TBCs have excellent thermal shock resistance.

Thermal cycling life is an important index to evaluate the practical performance of TBCs. Long thermal cycle life is more suitable for TBC candidates. There are many factors that affect the thermal cycle life, such as cooling rate, temperature, high-temperature dwell time, and so on. Under similar experimental conditions, the thermal cycling life of $La_2Zr_2O_7$/YSZ-TBC is 160 times, $GdPO_4$/YSZ-TBC is 70 times, and $(La_{0.8}Eu_{0.2})_2Zr_2O_7$/YSZ-TBC is 32 times [68–70]. The thermal cycling life of these new thermal barrier coatings is less than that of Gd–Sc/YSZ DCL TBCs. In particular, compared with $Gd_2Zr_2O_7$, the thermal cycling life is increased by 55% [71]. Therefore, Gd–Sc/YSZ TBCs have excellent thermal shock resistance and good application prospects in the newly developed thermal barrier coating materials.

4　Conclusions

In this work, the first-principles method is used to study the solid solution mechanisms of Sc atoms in $Gd_2Zr_2O_7$ lattice. The variation of mechanical and thermophysical properties of Sc-doped $Gd_2Zr_2O_7$ (Gd–Sc) with the Sc content is also investigated. Based on theoretical

calculation results, the Sc doping content was optimized. Then, Gd–Sc TBCs and Gd–Sc/YSZ TBCs were produced by air plasma spraying, and the phase composition, microstructure, sintering behavior, and thermal cycling performance of the coatings were investigated. Following conclusions can be drawn.

When the content of Sc is 5.88 at%, Sc atoms mainly occupy the interstitial sites in the $Gd_2Zr_2O_7$ lattice because the formation energy of interstitial doping is significantly lower than that of substitution doping. The variation trend of the lattice constant shows that the Sc interstitial concentration might be less than 11.11 at%. After that, Gd would be gradually replaced by Sc with the increase of the doping content.

Compared with $Gd_2Zr_2O_7$, Gd–Sc has lower Young's modulus and Pugh's indicator (G/B) and a higher Poisson ratio (σ) suggesting better thermal shock resistance and higher toughness. At a doping level of 16.67 at% Sc, Gd–Sc exhibited the lowest G/B and the highest σ indicative of the highest toughness. With the increase of the Sc content, the Debye temperature and thermal conductivity have similar variation trends, which have a significant decrease when doping 5.88 at% Sc, and then increase slightly followed by a decrease with further doping. When the Sc content exceeds 16.67 at%, the decreasing trend of Debye temperature and thermal conductivity slow down. Therefore, the Sc doping content in $Gd_2Zr_2O_7$ is optimized to be 16.67 at%.

Gd–Sc coatings maintain excellent phase and structural stability after heat treatment at 1400 ℃ for 100 h. The thermal shock resistance of Gd–Sc/YSZ DCL TBCs is better than that of Gd–Sc TBCs. Due to the improvement in the toughness and TEC and the decrease in Young's modulus, Gd–Sc coatings have good structural integrity and excellent matching with YSZ coating during thermal cycling. In addition, YSZ coating plays a good buffer role during thermal cycling and prevents the reaction of Gd–Sc with the bond coat. Gd–Sc coatings reveal excellent thermal shock resistance and sintering resistance, which has a promising application prospect.

Acknowledgements

References

[1] Guo H, Gong S, Xu H. Research progress on new high/ultra-high-temperature thermal barrier coatings and processing technologies. *Acta Aeronaut Astronaut Sin* 2014, **35**: 2722–2732.

[2] Vaßen R, Jarligo MO, Steinke T, *et al*. Overview on advanced thermal barrier coatings. *Surf Coat Technol* 2010, **205**: 938–942.

[3] Li DX, Jiang P, Gao RH, *et al*. Experimental and numerical investigation on the thermal and mechanical behaviours of thermal barrier coatings exposed to CMAS corrosion. *J Adv Ceram* 2021, **10**: 551–564.

[4] Kumar V, Balasubramanian K. Progress update on failure mechanisms of advanced thermal barrier coatings: A review. *Prog Org Coat* 2016, **90**: 54–82.

[5] Mauer G, Jarligo MO, Mack DE, *et al*. Plasma-sprayed thermal barrier coatings: New materials, processing issues, and solutions. *J Therm Spray Technol* 2013, **22**: 646–658.

[6] Rai AK, Schmitt MP, Bhattacharya RS, *et al*. Thermal conductivity and stability of multilayered thermal barrier coatings under high temperature annealing conditions. *J Eur Ceram Soc* 2015, **35**: 1605–1612.

[7] Guo L, Gao Y, Ye FX, *et al*. CMAS corrosion behavior and protection method of thermal barrier coatings for aeroengine. *Acta Metall Sin* 2021, **57**: 1184–1198. (in Chinese)

[8] Feuerstein A, Knapp J, Taylor T, *et al*. Technical and economical aspects of current thermal barrier coating systems for gas turbine engines by thermal spray and EBPVD: A review. *J Therm Spray Technol* 2008, **17**: 199–213.

[9] Zhao ZF, Chen H, Xiang HM, *et al*. High entropy defective fluorite structured rare-earth niobates and tantalates for thermal barrier applications. *J Adv Ceram* 2020, **9**: 303–311.

[10] Guo L, Li MZ, He SX, *et al*. Preparation and hot corrosion behavior of plasma sprayed nanostructured $Gd_2Zr_2O_7$–$LaPO_4$ thermal barrier coatings. *J Alloys Compd* 2017, **698**: 13–19.

[11] Zhao FA, Xiao HY, Liu ZJ, *et al*. A DFT study of mechanical properties, thermal conductivity and electronic structures of Th-doped $Gd_2Zr_2O_7$. *Acta Mater* 2016, **121**: 299–309.

[12] Zhao FA, Xiao HY, Bai XM, *et al*. Effects of doping Yb^{3+}, La^{3+}, Ti^{4+}, Hf^{4+}, Ce^{4+} cations on the mechanical properties, thermal conductivity, and electronic structures of $Gd_2Zr_2O_7$. *J Alloys Compd* 2019, **776**: 306–318.

[13] Zhang Y, Guo L, Zhao XX, *et al*. Toughening effect of Yb_2O_3 stabilized ZrO_2 doped in $Gd_2Zr_2O_7$ ceramic for thermal barrier coatings. *Mater Sci Eng*: A 2015, **648**: 385–391.

[14] Zhang CG, Fan Y, Zhao JL, *et al*. Corrosion resistance of non-stoichiometric gadolinium zirconate fabricated by laser-enhanced chemical vapor deposition. *J Adv Ceram* 2021, **10**: 520–528.

[15] Doleker KM, Karaoglanli AC. Comparison of oxidation

behavior of YSZ and Gd₂Zr₂O₇ thermal barrier coatings (TBCs). *Surf Coat Technol* 2017, **318**: 198–207.

[16] Vaßen R, Bakan E, Mack D, *et al*. Performance of YSZ and Gd₂Zr₂O₇/YSZ double layer thermal barrier coatings in burner rig tests. *J Eur Ceram Soc* 2020, **40**: 480–490.

[17] Sayed FN, Grover V, Bhattacharyya K, *et al*. Sm₂₋ₓDyₓZr₂O₇ pyrochlores: Probing Order−Disorder dynamics and multifunctionality. *Inorg Chem* 2011, **50**: 2354–2365.

[18] Kutty KVG, Rajagopalan S, Mathews CK, *et al*. Thermal expansion behaviour of some rare earth oxide pyrochlores. *Mater Res Bull* 1994, **29**: 759–766.

[19] Lee KS, Jung KI, Heo YS, *et al*. Thermal and mechanical properties of sintered bodies and EB-PVD layers of Y₂O₃ added Gd₂Zr₂O₇ ceramics for thermal barrier coatings. *J Alloys Compd* 2010, **507**: 448–455.

[20] Wang CM, Guo L, Zhang Y, *et al*. Enhanced thermal expansion and fracture toughness of Sc₂O₃-doped Gd₂Zr₂O₇ ceramics. *Ceram Int* 2015, **41**: 10730–10735.

[21] Guo L, Zhang Y, Wang CM, *et al*. Phase structure evolution and thermal expansion variation of Sc₂O₃ doped Nd₂Zr₂O₇ ceramics. *Mater Des* 2015, **82**: 114–118.

[22] Zhang CL, Li MZ, Zhang YC, *et al*. Hot corrosion behavior of (Gd₀.₉Sc₀.₁)₂Zr₂O₇ in V₂O₅ molten salt at 700–1000 ℃. *Ceram Int* 2017, **43**: 9041–9046.

[23] Karabaş M. Production and characterization of Nd and Dy doped lanthanum zirconate-based thermal barrier coatings. *Surf Coat Technol* 2020, **394**: 125864.

[24] Zhang HL, Guo L, Ma Y, *et al*. Thermal cycling behavior of (Gd₀.₉Yb₀.₁)₂Zr₂O₇/8YSZ gradient thermal barrier coatings deposited on Hf-doped NiAl bond coat by EB-PVD. *Surf Coat Technol* 2014, **258**: 950–955.

[25] Bahamirian M, Hadavi SMM, Farvizi M, *et al*. Thermal durability of YSZ/nanostructured Gd₂Zr₂O₇ TBC undergoing thermal cycling. *Oxid Met* 2019, **92**: 401–421.

[26] Shen ZY, He LM, Xu ZH, *et al*. LZC/YSZ DCL TBCs by EB-PVD: Microstructure, low thermal conductivity and high thermal cycling life. *J Eur Ceram Soc* 2019, **39**: 1443–1450.

[27] Zhou FF, Wang Y, Cui ZY, *et al*. Thermal cycling behavior of nanostructured 8YSZ, SZ/8YSZ and 8CSZ/8YSZ thermal barrier coatings fabricated by atmospheric plasma spraying. *Ceram Int* 2017, **43**: 4102–4111.

[28] Liu B, Zhao JL, Liu YC, *et al*. Application of high-throughput first-principles calculations in ceramic innovation. *J Mater Sci Technol* 2021, **88**: 143–157.

[29] Li YM, Meng X, Chen Q, *et al*. Electronic structure and thermal properties of Sm³⁺-doped La₂Zr₂O₇: First-principles calculations and experimental study. *J Am Ceram Soc* 2021, **104**: 1475–1488.

[30] Kresse G, Furthmüller J. Efficient iterative schemes for *ab initio* total-energy calculations using a plane-wave basis set. *Phys Rev B Condens Matter* 1996, **54**: 11169–11186.

[31] Kresse G, Furthmüller J. Efficiency of ab-initio total energy calculations for metals and semiconductors using a plane-wave basis set. *Comput Mater Sci* 1996, **6**: 15–50.

[32] Perdew JP, Burke K, Wang Y. Generalized gradient approximation for the exchange-correlation hole of a many-electron system. *Phys Rev B Condens Matter* 1996, **54**: 16533–16539.

[33] Zhao FA, Xiao HY, Bai XM, *et al*. Effects of Nd doping on the mechanical properties and electronic structures of Gd₂Zr₂O₇: A first-principles-based study. *J Mater Sci* 2018, **53**: 16423–16438.

[34] Feng J, Xiao B, Wan CL, *et al*. Electronic structure, mechanical properties and thermal conductivity of Ln₂Zr₂O₇ (Ln = La, Pr, Nd, Sm, Eu and Gd) pyrochlore. *Acta Mater* 2011, **59**: 1742–1760.

[35] Yang L, Wang PY, Zhang CG, *et al*. Composition-dependent intrinsic defect structures in pyroclore RE₂B₂O₇ (RE = La, Nd, Gd; B = Sn, Hf, Zr). *J Am Ceram Soc* 2020, **103**: 645–655.

[36] Guo L, Li G, Gan ZL. Effects of surface roughness on CMAS corrosion behavior for thermal barrier coating applications. *J Adv Ceram* 2021, **10**: 472–481.

[37] Zhu RB, Zou JP, Mao J, *et al*. Fabrication and growing kinetics of highly dispersed gadolinium zirconate nanoparticles. *Res Appl Mater Sci* 2019, **1**: 45–54.

[38] Lumpkin GR, Pruneda M, Rios S, *et al*. Nature of the chemical bond and prediction of radiation tolerance in pyrochlore and defect fluorite compounds. *J Solid State Chem* 2007, **180**: 1512–1518.

[39] Jiang C, Stanek CR, Sickafus KE, *et al*. First-principles prediction of disordering tendencies in pyrochlore oxides. *Phys Rev B* 2009, **79**: 104203.

[40] Luo F, Li BS, Guo ZC, *et al*. Ab initio calculation of mechanical and thermodynamic properties of Gd₂Zr₂O₇ pyrochlore. *Mater Chem Phys* 2020, **243**: 122565.

[41] Wang XJ, Xiao HY, Zu XT, *et al*. Study of cerium solubility in Gd₂Zr₂O₇ by DFT + U calculations. *J Nucl Mater* 2011, **419**: 105–111.

[42] Lu XR, Shu XY, Wang L, *et al*. Microstructure evolution of rapidly fabricated Gd₂₋ₓNdₓZr₂O₇ (0.0 ≤ *x* ≤ 2.0) by spark plasma sintering. *Ceram Int* 2018, **44**: 2458–2462.

[43] Lu XR, Dong FQ, Song GB, *et al*. Phase and rietveld refinement of pyrochlore Gd₂Zr₂O₇ used for immobilization of Pu (IV). *J Wuhan Univ Technol Mater Sci Ed* 2014, **29**: 233–236.

[44] Wang YH, Li YH, Liu CG, *et al*. First-principles study of plutonium and cerium solubility in Gd₂Sn₂O₇ pyrochlore. *Nucl Instrum Methods Phys Res Sect B*: *Beam Interact Mater Atoms* 2018, **436**: 211–216.

[45] Van de Walle CG, Neugebauer J. First-principles calculations for defects and impurities: Applications to III-nitrides. *J Appl Phys* 2004, **95**: 3851–3879.

[46] Zhang J, Chen X, Deng M, *et al*. Effects of native defects and cerium impurity on the monoclinic BiVO₄ photocatalyst obtained via PBE+U calculations. *Phys Chem Chem Phys* 2020, **22**: 25297–25305.

[47] Wang JH, Yip S, Phillpot SR, *et al*. Crystal instabilities at finite strain. *Phys Rev Lett* 1993, **71**: 4182–4185.

[48] Wan CL, Pan W, Xu Q, *et al*. Effect of point defects on the thermal transport properties of$(La_xGd_{1-x})_2Zr_2O_7$: Experiment and theoretical model. *Phys Rev B* 2006, **74**: 144109.

[49] Thompson JA, Clyne TW. The effect of heat treatment on the stiffness of zirconia top coats in plasma-sprayed TBCs. *Acta Mater* 2001, **49**: 1565–1575.

[50] Pugh SF. XCII. Relations between the elastic moduli and the plastic properties of polycrystalline pure metals. *The London, Edinburgh, and Dublin Philosophical Magazine and Journal of Science* 1954, **45**: 823–843.

[51] Haines J, Léger JM, Bocquillon G. Synthesis and design of superhard materials. *Annu Rev Mater Res* 2001, **31**: 1–23.

[52] Shimamura K, Arima T, Idemitsu K, *et al*. Thermophysical properties of rare-earth-stabilized zirconia and zirconate pyrochlores as surrogates for actinide-doped zirconia. *Int J Thermophys* 2007, **28**: 1074–1084.

[53] Childress JR, Chien CL, Zhou MY, *et al*. Lattice softening in nanometer-size iron particles. *Phys Rev B* 1991, **44**: 11689–11696.

[54] Wu J, Wei XZ, Padture NP, *et al*. Low-thermal-conductivity rare-earth zirconates for potential thermal-barrier-coating applications. *J Am Ceram Soc* 2002, **85**: 3031–3035.

[55] Maloney MJ. Thermal barrier coating systems and materials. United States Patent 6,177,200, Jan. 2001.

[56] Suresh G, Seenivasan G, Krishnaiah MV, *et al*. Investigation of the thermal conductivity of selected compounds of gadolinium and lanthanum. *J Nucl Mater* 1997, **249**: 259–261.

[57] Han WD, Li K, Dai J, *et al*. Structural, mechanical, and thermodynamic properties of newly-designed superhard carbon materials in different crystal structures: A first-principles calculation. *Comput Mater Sci* 2020, **171**: 109229.

[58] Yang J, Feng J, Zhao M, *et al*. Electronic structure, mechanical properties and anisotropy of thermal conductivity of Y–Si–O–N quaternary crystals. *Comput Mater Sci* 2015, **109**: 231–239.

[59] Chong XY, Jiang YH, Zhou R, *et al*. Stability, chemical bonding behavior, elastic properties and lattice thermal conductivity of molybdenum and tungsten borides under hydrostatic pressure. *Ceram Int* 2016, **42**: 2117–2132.

[60] Clarke DR. Materials selection guidelines for low thermal conductivity thermal barrier coatings. *Surf Coat Technol* 2003, **163–164**: 67–74.

[61] Kittel C. Interpretation of the thermal conductivity of glasses. *Phys Rev* 1949, **75**: 972–974.

[62] Wan CL, Zhang W, Wang YF, *et al*. Glass-like thermal conductivity in ytterbium-doped lanthanum zirconate pyrochlore. *Acta Mater* 2010, **58**: 6166–6172.

[63] Li XB. Investigation of cold sprayed NiCoCrAlY bond coating. *Adv Mater Res* 2009, **79–82**: 863–866.

[64] Ul-Hamid A, Dafalla H, Al-Yousef F, *et al*. Microstructural study of NiCrAlY electrodeposits. *Prot Met Phys Chem Surf* 2014, **50**: 679–687.

[65] Leckie RM, Krämer S, Rühle M, *et al*. Thermochemical compatibility between alumina and ZrO_2–$GdO_{3/2}$ thermal barrier coatings. *Acta Mater* 2005, **53**: 3281–3292.

[66] Zhao D, An Y, Zhao X, *et al*. Structure and properties of 8YSZ thermal barrier coatings with different thickness. *Surf Technol* 2020, **49**: 276–284.

[67] Su L, Wu H, Lei X, *et al*. Effect of thickness of bond coat on the life of TBCs in EB-PVD process. *Rare Met Mater Eng* 2012, **41**: 417–420.

[68] Jin G, Fang YC, Cui XF, *et al*. Effect of YSZ fibers and carbon nanotubes on bonding strength and thermal cycling lifetime of YSZ–$La_2Zr_2O_7$ thermal barrier coatings. *Surf Coat Technol* 2020, **397**: 125986.

[69] Guo L, Yan Z, Li ZH, *et al*. $GdPO_4$ as a novel candidate for thermal barrier coating applications at elevated temperatures. *Surf Coat Technol* 2018, **349**: 400–406.

[70] Liu ZG, Zhang WH, Ouyang JH, *et al*. Novel double-ceramic-layer $(La_{0.8}Eu_{0.2})_2Zr_2O_7$/YSZ thermal barrier coatings deposited by plasma spraying. *Ceram Int* 2014, **40**: 11277–11282.

[71] Karaoglanli AC, Doleker KM, Ozgurluk Y. Interface failure behavior of yttria stabilized zirconia (YSZ), $La_2Zr_2O_7$, $Gd_2Zr_2O_7$, YSZ/$La_2Zr_2O_7$ and YSZ/$Gd_2Zr_2O_7$ thermal barrier coatings (TBCs) in thermal cyclic exposure. *Mater Charact* 2020, **159**: 110072.